Increased Surface Temperatures of Habitable White Dwarf Worlds Relative to Main-sequence Exoplanets

Aomawa L. Shields[1] , Eric T. Wolf[2] , Eric Agol[3] , and Pier-Emmanuel Tremblay[4]
[1] Department of Physics and Astronomy, University of California, Irvine, 4129 Frederick Reines Hall, Irvine, CA 92697-4575, USA; shields@uci.edu
[2] Laboratory for Atmospheric and Space Physics, University of Colorado, Boulder, CO 80303, USA
[3] Department of Physics and Astronomy, University of Washington, Seattle, WA 98105-6698, USA
[4] Department of Physics, University of Warwick, Coventry, CV4 7AL, UK

Abstract

Discoveries of giant planet candidates orbiting white dwarf (WD) stars and the demonstrated capabilities of the James Webb Space Telescope bring the possibility of detecting rocky planets in the habitable zones (HZs) of WDs into pertinent focus. We present simulations of an aqua planet with an Earth-like atmospheric composition and incident stellar insolation orbiting in the HZ of two different types of stars—a 5000 K WD and main-sequence K-dwarf star Kepler-62 (K62) with a similar effective temperature—and identify the mechanisms responsible for the two differing planetary climates. The synchronously rotating WD planet's global mean surface temperature is 25 K higher than that of the synchronously rotating planet orbiting K62, due to its much faster (10 hr) rotation and orbital period. This ultrafast rotation generates strong zonal winds and meridional flux of zonal momentum, stretching out and homogenizing the scale of atmospheric circulation, and preventing an equivalent buildup of thick, liquid water clouds on the dayside of the planet compared to the synchronous planet orbiting K62, while also transporting heat equatorward from higher latitudes. White dwarfs may therefore present amenable environments for life on planets formed within or migrated to their HZs, generating warmer surface environments than those of planets with main-sequence hosts to compensate for an ever shrinking incident stellar flux.

Unified Astronomy Thesaurus concepts: Planetary climates (2184); White dwarf stars (1799); Astrobiology (74)

1. Introduction

White dwarf (WD) stars are the final, electron-degenerate core phase of evolution for most stars in the Galaxy. During the dramatic red giant phase of stellar evolution, the outer shell of a lower-mass main-sequence star blows outwards, presumably engulfing any planets in or interior to the habitable zone (HZ) of their progenitor, and leaving behind a small remnant stellar core. To date only giant planet candidates have been discovered around WDs (K. L. Luhman et al. 2011; B. T. Gänsicke et al. 2019; A. Vanderburg et al. 2020; J. W. Blackman et al. 2021; S. E. Mullally et al. 2024). Potentially rocky planets have also been found at large orbital distances from the WD in a system containing a pulsar, a rocky planet, and a WD (S. E. Thorsett et al. 1993; S. Sigurdsson et al. 2003), and a system containing a WD, rocky planet, and a brown dwarf (K. Zhang et al. 2024). Detections of circumstellar debris disk material at close and moderate orbital distances from WDs (M. Jura 2003; A. Vanderburg et al. 2015; Z. Vanderbosch et al. 2020; J. Farihi et al. 2022; A. Aungwerojwit et al. 2024; A. Swan et al. 2024) bolster the possibility that small, rocky planets may orbit in the HZs of these post-main-sequence stars (D. Veras 2021), even though these planets may be rare (D. Kipping 2024), having arrived subsequent to the red giant phase (e.g., J. Nordhaus et al. 2010), either through inward migration (J. H. Debes & S. Sigurdsson 2002) or forming from the gas surrounding the WD (M. Livio et al. 2005).

Unlike main-sequence stars, WDs continue to cool with time, resulting in a white dwarf habitable zone (WDHZ) that is extremely close to the star and inwardly migrating, while sustaining planets within its boundaries for up to 8 Gyr (E. Agol 2011a, 2011b). However, long-term habitability in these systems depends on several factors. The most relevant habitability factors include the age and cooling time of the WD (J. P. Ostriker & L. Axel 1968), the incident stellar radiation at close orbital distances, which could cause orbiting planets to lose their water inventories to space in a runaway greenhouse phase at or near the inner edge of the WDHZ (R. Barnes & R. Heller 2013), the ultraviolet (UV) radiation dosage and surface environment, as well as requisite shielding of an orbiting planet's atmosphere (see, e.g., L. Fossati et al. 2012; T. Kozakis et al. 2018; J. Gertz 2019), and the location of a planet within the WDHZ relative to the WD's Roche limit, within which tides will deform and possibly disrupt an orbiting planet (D. M. Williams & D. Pollard 2003).

The climate and habitability of planets are also affected by their rotation rate (see, e.g., A. Edson et al. 2011; E. S. Kite et al. 2011; A. P. Showman et al. 2013; Y. Hu & J. Yang 2014; Y. Wang et al. 2014a, 2014b; Y. Kaspi & A. P. Showman 2015; S. D. Guzewich et al. 2020; A. H. Lobo et al. 2023), as well as the interaction between the spectral energy distribution (SED) of their host stars and the wavelength-dependent albedos of planetary surfaces (A. L. Shields et al. 2013, 2014; A. L. Shields & R. C. Carns 2018; A. J. Rushby et al. 2019, 2020; I. Palubski et al. 2020). Given the close orbital distances of WDHZ planets, such planets are highly likely to be synchronously rotating, with much faster orbital and rotation periods compared to synchronously rotating HZ planets orbiting brighter, main-sequence stars, leading to major differences in atmospheric circulation and heat distribution around the planet, depending on atmospheric composition (see, e.g., R. D. Wordsworth et al. 2010). The SEDs of WDs, which

have ceased to undergo core nuclear fusion—apart from varying degrees of residual thermonuclear burning in the hydrogen-rich envelopes of low-metallicity ($Z < 0.001$) WDs; see, e.g., J. Chen et al. (2021)—will also differ from those of main-sequence stars with equivalent effective temperatures. Additionally, the atmospheric composition of WDs can change substantially as they cool, resulting in an evolution of their spectral properties and appearance over time (A. Bédard et al. 2020, 2022). As such, the interaction between the WD SED and an orbiting planet's surface, and the resulting climatic effect on the planet, will also differ correspondingly. Studies have identified an infrared (IR) deficit in select samples of the WD stellar population (P. Bergeron et al. 1995a; B. R. Oppenheimer et al. 2001), which could affect the interaction between the WD SED and any water ice and snow on orbiting planets, as these surfaces have wavelength-dependent albedo properties, with much lower albedos in the IR (R. V. Dunkle & J. T. Bevans 1956). The effect of WD host stars on the climate and habitability of potential orbiting Earth-sized planets has not been widely explored. Given the potential capabilities of the James Webb Space Telescope (JWST; J. P. Gardner et al. 2006; J. Kalirai 2018) to characterize atmospheres of Earth-sized planets around WDs (A. Loeb & D. Maoz 2013; L. Kaltenegger et al. 2020; Z. Lin et al. 2022), quantifying the climatic impact on surface habitability of the specific stellar environment of these planets is of imminent relevance.

In this work, we explore and compare the climate of a simulated aqua planet (no land) with an Earth-like atmospheric composition and incident stellar insolation (hereafter "instellation") orbiting in the HZ of a 5000 K pure-hydrogen atmosphere WD with that of a planet receiving an equivalent instellation from a main-sequence star with a similar effective temperature, Kepler-62 (4859 K).[5] While the different formation and evolutionary histories of these two planets would likely result in different interior and atmospheric compositions, their compositions are assumed to be equivalent in this study, to isolate the climatic effects of the planetary rotation and orbital period given the HZ location of each host star. In Section 2, we present and explain our methods and models used to undertake this study. In Sections 3 and 4, we present and discuss the results and significance of our simulated planets' climates in the context of their habitability potential given their different stellar host environments. In Section 5, we offer concluding remarks and implications of this work for future studies of the potential climates of terrestrial planets discovered around WD stars.

2. Methods and Models

We used the Community Earth System Model (CESM) version 1.2.1, a three-dimensional (3D) global climate model (GCM) developed to simulate past and present climate states on the Earth (P. R. Gent et al. 2011), with ExoCAM (E. T. Wolf et al. 2022), which is a modified version of the atmospheric component to CESM, the Community Atmosphere Model (CAM4), and the Los Alamos sea-ice model (CICE, version 4; E. C. Hunke & W. H. Lipscomb 2008). ExoCAM employs a correlated-k radiative transfer code (ExoRT), and a finite-volume dynamical core. A complete description of the code and its lineage is available in E. T. Wolf et al. (2022). The

ocean is treated as static, but fully mixed with depth. Simulations that include a fully dynamic ocean are too computationally expensive to permit the in-depth exploration of the forcing parameters we prioritize in this work. The horizontal resolution is $4° \times 5°$. We increased the horizontal resolution to $2° \times 2°.5$ in select sensitivity tests to confirm that Rossby waves were resolvable at the rotation rate of the WD planet ($\sim$10 hr), and calculated that the climates were equivalent to those run at the lower resolution. We therefore ran our full suite of simulations at $4° \times 5°$ to reduce computational expense. Simulations of planets with similar rotation periods were run at this resolution in previous work (T. D. Komacek et al. 2019). We simulated the climates of aqua planets (no land) orbiting two stars with similar effective temperatures, a modeled WD (5000 K) and Kepler-62 (4859 K). We chose this effective temperature for the WD because 5000 K is near the peak of the WD luminosity distribution (D. E. Winget et al. 1987), the duration within the WDHZ is at a maximum ($\sim$8 Gyr) at the 10 hr orbital period of a planet receiving Earth-like instellation from a WD at this temperature, and such a planet would be well outside of the Roche limit (E. Agol 2011a, 2011b).

We created a synthetic spectrum of Kepler-62 (K62) using a surface gravity $\log(g) = 4.59$, metallicity Fe/H $= -0.34$, and effective temperature $T_{\text{eff}} = 4859$ K from the NASA Exoplanet Archive.[6] The mass $M = 0.697 M_\odot$ and radius $R = 0.707 R_\odot$ from isochrone fitting yield a luminosity $L = 0.25 L_\odot$ from Fulton and Petigura (B. J. Fulton & E. A. Petigura 2018). The synthetic spectrum for the WD was obtained from a grid of synthetic spectra and cooling models for WDs with pure-hydrogen atmospheres based on previous calculations (P. Bergeron et al. 1995b; P. M. Kowalski & D. Saumon 2006; P. E. Tremblay et al. 2011).[7] The WD spectrum assumed a surface gravity $\log(g) = 8.0$ and $T_{\text{eff}} = 5000$ K. This corresponds to an age of 5.96 Gyr, mass $M = 0.580 M_\odot$, and radius $R = 0.012 R_\odot$, yielding a luminosity $L = 8.87 \times 10^{-5} L_\odot$, based on the evolutionary cooling sequences provided by A. Bédard et al. (2020). The synthetic spectra of both host stars are provided in Figure 1.

We assumed circular orbits for our orbiting planets, Earth's radius, mass, atmospheric composition, and surface pressure. The planets were assumed to be synchronously rotating, as defined as tidally locked in a 1:1 spin–orbit resonance. Each planet was put at the distance from its host star where it would receive an Earth-like equivalent amount of instellation ($\sim$1360 W m^{-2}), given the host star's intrinsic stellar luminosity. For the simulated planets around K62 and the WD, these distances corresponded to 0.50 au and 0.01 au, respectively. Rotation periods were then calculated for each planet based on Kepler's third law. The majority of the simulations were carried out assuming synchronous rotation periods of 155 days and 0.44 days, assuming the K62 and WD host stars, respectively. Simulations were run until thermal equilibrium was reached, where global mean surface temperatures were stable within $1°$ over the last 20 model years. Atmospheric water vapor was allowed to vary during each simulation according to evaporation and precipitation processes on the surface and in the atmosphere.

---

[5] The simulated Kepler-62 planet corresponds to a hypothetical planet whose orbit would lie in between those of Kepler-62 e and Kepler-62 f.

[6] https://exoplanetarchive.ipac.caltech.edu/overview/Kepler-62/

[7] https://warwick.ac.uk/fac/sci/physics/research/astro/people/tremblay/modelgrids/
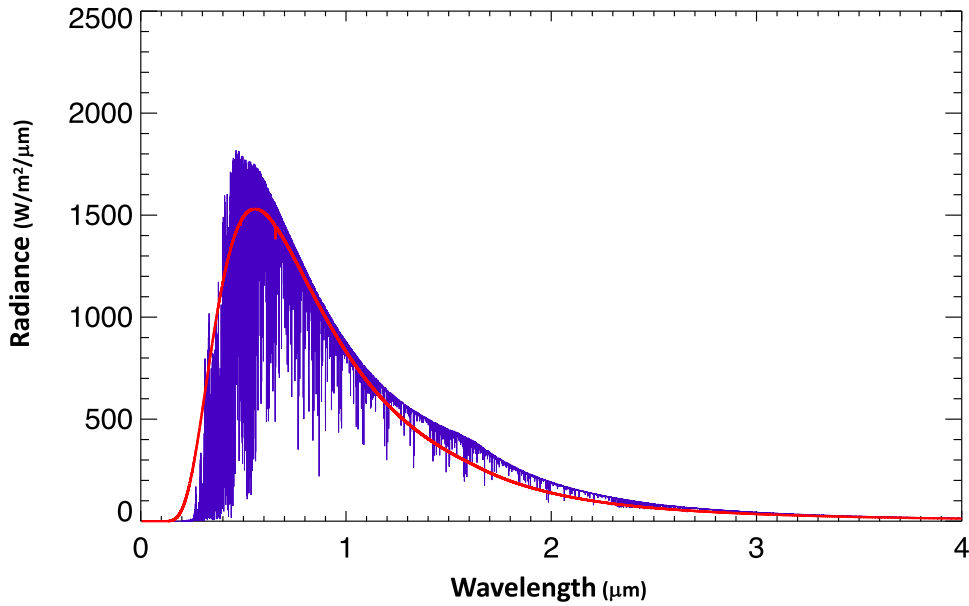
Figure 1. The spectral energy distribution of a modeled WD with an effective temperature of 5000 K (red) and a synthetic spectrum of Kepler-62 (4859 K, purple). Both SEDs have been normalized to an Earth-like instellation (~1360 W m^{-2}).

Table 1
Two-band Albedos Employed for Different Temperature Regimes (Given in Degrees Celsius) Reached in the GCM, Weighted by the Spectrum for K-dwarf Star K62 (4859 K) and a Modeled WD (5000 K)

Host star	$0° > T > -23°$	$-23° > T > -40°$	$T < -40°$	$E - P < 0$
Band	Near-IR/VIS	Near-IR/VIS	Near-IR/VIS	Near-IR/VIS
K62	0.20/0.69	0.24/0.81	0.89/0.95	0.55/0.98
WD	0.21/0.70	0.26/0.82	0.90/0.95	0.59/0.98

Note. E and P denote water evaporation and precipitation, respectively. Where $E - P < 0$, albedos for dry snow are employed.

Given that previous work has shown that the observed planet Kepler-62 f, with a 267 day orbital period, could have reached tidal circularization within the 7 Gyr age of the system (A. L. Shields et al. 2016), and other work also shows that it is possible with current models for our hypothetical K62 planet to orbit within the tidal locking radius (R. Barnes 2017), it is reasonable to assume synchronous rotation for the planet in this study. However, as rotational state can vary across a range of rotation periods (see, e.g., J. Yang et al. 2014), and processes such as atmospheric tides could counteract gravitational inducements toward synchronous rotation (J. Leconte et al. 2015), we also simulated the potential climate of the K62 planet in a nonsynchronous case, by prescribing a 10 hr rotation period as with the WD planet, while leaving its orbital period at 155 days to allow for an additional comparison of the climates of these two planets in an equivalent rotation period scenario.

The sea-ice albedo parameterization used with ExoCAM divides the surface albedo into two bands (as done in A. L. Shields et al. 2013, 2014, 2016), visible ($\lambda \leqslant 0.751880\,\mu$m) and near-IR ($\lambda > 0.751880\,\mu$m), because it is easier to control than the multiple-scattering scheme in other code versions. The default near-IR and visible band albedos are 0.3 and 0.67 for bare water ice and 0.68 and 0.8 for dry snow, respectively, assuming the Sun as the host star. For our simulations of the climates of planets orbiting the K-dwarf star K62 and the modeled WD, we calculated the two-band albedos weighted by the specific spectrum of each host star, and used those values (Table 1) as input.

Modifications were made to the ice thermal code in CICE4, based on the original model written by C. M. Bitz et al. (2001), to incorporate the bare sea-ice albedo change due to the crystallization of hydrohalite at low temperatures, and the subsequent formation of a hydrohalite crust (see, e.g., R. C. Carns et al. 2015, 2016; B. Light et al. 2016), as done in previous simulations of exoplanet climates (A. L. Shields & R. C. Carns 2018). In the model, sea ice is allowed to form as surface temperatures reach the freezing point of liquid water. Areas of net water precipitation were assigned two-band albedos for salt-free snow with 100 μm-sized grains. For temperatures between freezing and the temperature where hydrohalite begins to precipitate in sea ice ($T < -23°$C), we used two-band albedos for salt-free, "warm" bare ice; below $-23°$C, we used two-band albedos for cold bare ice with precipitated hydrohalite; and below $-40°$C, we used two-band albedos for a fully formed hydrohalite crust. The two-band albedos weighted by the spectrum of each host star and used for each temperature regime are given in Table 1.

For temperature regimes where a hydrohalite crust was expected to form ($T < -40°$C), we altered the emissivity from a value of 1 for both salt-free water ice and snow, as well as cold bare ice with precipitated hydrohalite (99% H_2O and 1% NaCl), to 0.752—a weighted average between that of salt-free H_2O snow and fine-grained halite (60% in the thermal IR; M. D. Lane & P. R. Christensen 1998)—to approximate with greater accuracy the emissivity of a hydrohalite crust (62% NaCl and 38% H_2O by weight). We found this change in

emissivity to be relevant in our simulations given an Earth-like atmospheric composition, as temperatures reached below the hydrohalite crust formation threshold in the polar regions and wider on these planets, resulting in changes in their global mean surface temperatures of as much as 2° K in simulations with the temperature-dependent emissivity parameterization applied.

3. Results

Figure 2 shows surface temperature, top-of-atmosphere (TOA) albedo, surface albedo, and snow depth across synchronously rotating planets with an Earth-like composition receiving Earth-like instellation from each star in our study. The planet orbiting K62, with its 155 day rotation and orbital period, shows a characteristic, oval-shaped temperature pattern (Figure 2(A)), with the hottest point occurring at the substellar point on the planet's dayside, cooler temperatures occupying successive annuli outward from this point, and a cold nightside. In contrast, the synchronous WD planet, with its 10 hr rotation and orbital period, exhibits a distinctive pattern, with extended and stretched out scales of circulation across the planet and midlatitude jets, with the hottest surface temperatures located in these regions, similar to what is seen in simulations of other short-period planets (see, e.g., J. Haqq-Misra et al. 2018; T. D. Komacek & D. S. Abbot 2019; R. Zhan et al. 2024).

The jets seen on the WD planet exhibit homogeneity in temperature across the day/night boundary. In particular, the WD planet has a jet band across the pole from day- to nightside, and a minimum surface temperature at the dayside pole of the planet that is equivalent to its nightside minimum surface temperature. On the synchronous K62 planet, the nightside gets much colder than the pole of its dayside, with a minimum surface temperature that is 9° cooler than the dayside minimum. The overall nightside hemisphere mean surface temperature is $\sim$36 K colder than that of the WD planet.

On the slower-rotating K62 planet, large dayside cloud coverage centers around the substellar point, contributing to a high TOA albedo (Figure 2(B)). The WD planet has a TOA albedo that is 18% lower and is noticeably warmer, with a maximum surface temperature that is 18° higher (314 K) than that on the K62 planet and a global mean surface temperature $\sim$25 K higher. As K62 is a slightly cooler star than the WD, it emits more flux at longer wavelengths, which water ice and snow absorb more strongly compared to visible and near-UV radiation (see, e.g., M. M. Joshi & R. M. Haberle 2012; A. L. Shields et al. 2013, 2014). The effects of the wavelength-dependent albedo of water ice are seen at the poles of the two planets, with the K62 planet exhibiting darker ice at the poles (Figure 2(C)) compared to the poles of the WD planet, which have high-albedo thick snow in these regions (Figure 2(D)). Relevant values for surface temperature, TOA albedo, and ice fraction are given in Table 2.

The effects of the large difference in rotation period between the two planets are evident in the resulting atmospheric cloud patterns as shown in Figure 3. While the K62 planet has noticeably more clouds on the dayside than the nightside (Figure 3(A)), the WD planet has a fairly uniform cloud fraction day to night, with a similar jet-like pattern to the surface temperature pattern seen in Figure 2(B). The WD planet has a slightly larger dayside column-integrated cloud fraction than the synchronous K62 planet. However, a closer look at the contribution of individual cloud mass to the total cloud fraction

reveals a different trend. In spite of the WD planet's higher surface temperatures, the synchronous K62 planet has 20% more dayside liquid water cloud mass (Figure 3(B)), which contributes to the higher TOA albedo and stronger (greater net negative) incoming stellar, or "shortwave" (SW), cloud forcing (SWCF) on the K62 planet (Figure 3(C) and Table 2).

The decreased cloud fraction throughout most of the atmospheric column on the dayside of the WD planet (Figure 4(A)) decreases the amount of SW absorption and heating in the upper atmosphere, allowing more SW radiation to make it through the atmosphere, contributing to the increased temperatures on the surface of the WD planet (Figure 4(B)). This effect is amplified further on the nightside, where the WD planet's surface is even warmer than that of the K62 planet. A comparison of the longwave (LW) cloud forcing (LWCF) on the nightside, which indicates the contribution of clouds to a planet's greenhouse effect, reveals the synchronous K62 planet to be emitting on average $\sim$18 W m^{-2} more radiation to space on its nightside than the WD planet (Figure 5), further reducing temperatures.

The WD planet exhibits much stronger zonal winds and meridional flux of zonal eddy momentum compared to its synchronous counterpart orbiting K62. In contrast to the K62 planet's symmetrical pattern, strong phase tilts of the meridional flux of zonal momentum are seen above and below the equator on the WD planet (Figure 6). These phase tilts are in the directions northeast–southwest in the northern hemisphere and northwest–southeast in the southern hemisphere. The net result of these stronger areas of phase tilt is the transport of moisture from higher latitudes toward the equator, with local minima in the regions of convergence of phase-tilted meridional flux as well as along the midlatitude zonal wind jets, and local maxima along the phase-tilted directions north and south of the equator, increasing surface temperatures in those regions. The substantially lower meridional flux of zonal momentum on the slow-rotating K62 planet and minimal zonal wind strength contribute to the planet's large cloud fraction, which is relatively uniform and centered at the substellar point.

The synchronous WD and K62 planets exhibit strong and almost opposing zonal wind patterns, as shown in Figure 7. Equatorial superrotation is present throughout the atmospheric column on the K62 planet. On the fast-rotating WD planet, the maxima in zonal momentum flux westward of the substellar point inform the zonal wind pattern, which indicates westward subrotation throughout most of the atmospheric column at the equator and subtropics, up to $\sim$40°. A small region of eastward equatorial superrotation is present from $\sim$500 mb down to the surface, and in the upper latitudes throughout the troposphere, similar to what is seen in other recent work, and governed largely by the hotter midlatitudes compared to the equator, resulting in reversed low-latitude jets from eastward to westward outside of the equatorial regions (R. Zhan et al. 2024).

3.1. Climate Comparison with a Nonsynchronous K62 Planet

We also compared the resulting climates of both planets at equivalent rotation periods of 10 hr. The WD planet is therefore synchronous, while the K62 planet is nonsynchronous. The most notable differences are shown in Figure 8, with complete climate variable data listed in Table 2 alongside that of the synchronous planets.

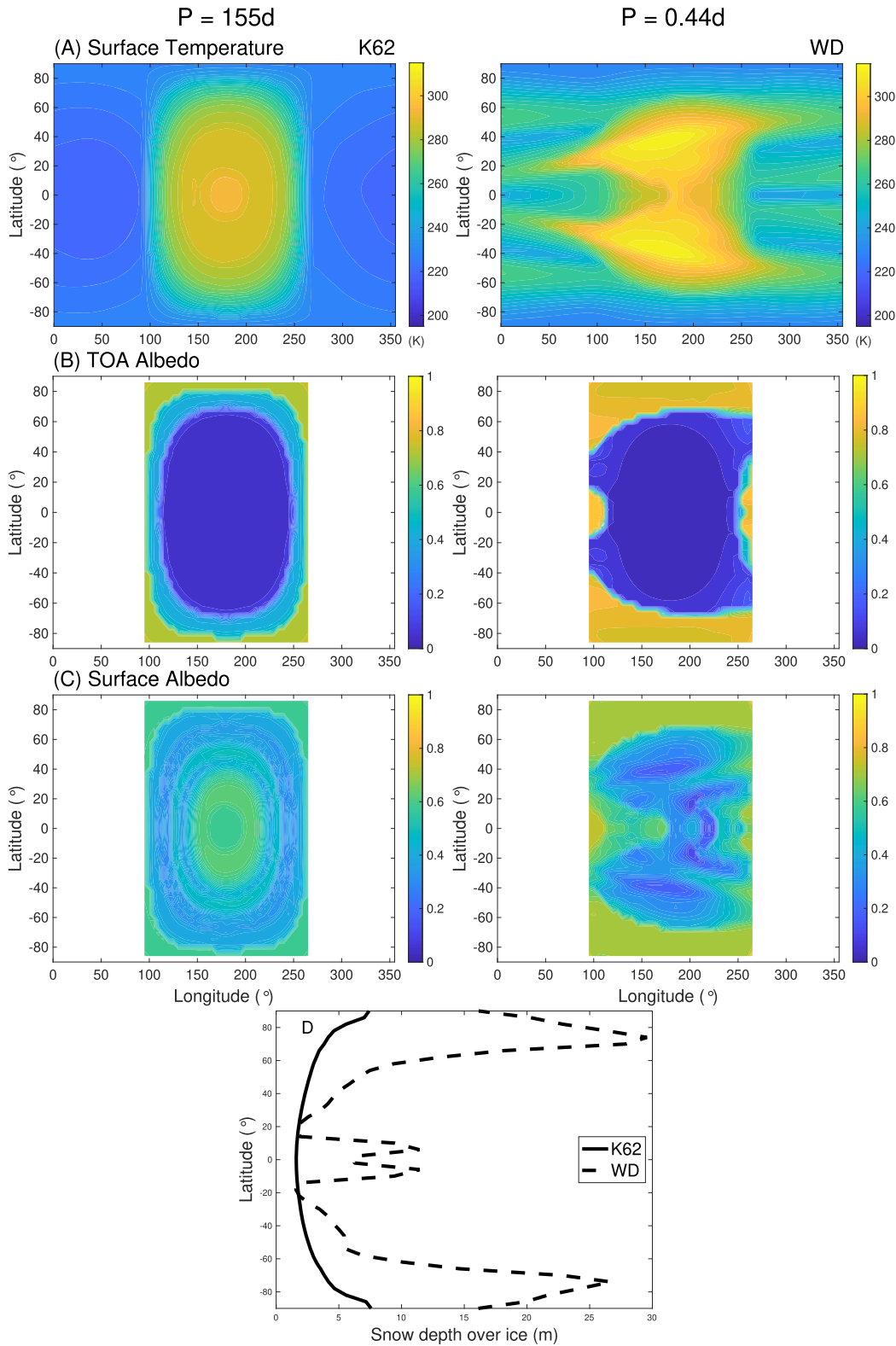As shown in Figure 8(A), the nonsynchronous planet orbiting K62, with a 10 hr rotation period and a 155 days

Figure 2. Climate comparisons for synchronously rotating planets with Earth-like atmospheric compositions receiving 100% of the modern solar constant from K62 and a 5000 K synthetic WD. Figure 2(D) is averaged over longitude. The slower-rotating K62 planet exhibits an oval-shaped temperature pattern with the hottest regions at the substellar point, high top-of-atmosphere (TOA) albedo due to large substellar cloud coverage, lower-albedo ice at the polar regions relative to the WD planet, and a cold nightside. The WD planet exhibits a lower TOA albedo and higher-albedo thick snow at the poles, while its ultrafast rotation generates a more homogeneous appearance between day- and nightsides, midlatitude jets, and a banded pattern, yielding hotter surface temperatures in these regions, with a global mean surface temperature ~25 K higher than on the K62 planet.

orbital period, exhibits a surface temperature pattern quite different from either of the synchronous planets. Its pattern is longitudinally homogeneous, similar to rapidly rotating long-

orbital-period planets like the Earth, with warm tropical and midlatitude regions and cooler temperatures in the upper latitudes and at the poles. On the nonsynchronous K62 planet,

Table 2
Model Inputs (Above Single Solid Line) and Climate Data (Below Single Solid Line) for Simulations of Earth-sized Planets Orbiting Kepler-62 and a Modeled 5000 K White Dwarf

Host star	K62 (sync)	WD (sync)	K62 (nonsync)
Instellation (W/m^2)	1361.27	1361.27	1361.27
Atmospheric composition	367 ppmv CO$_2$	367 ppmv CO$_2$	367 ppmv CO$_2$
	1.76 ppmv CH$_4$	1.76 ppmv CH$_4$	1.76 ppmv CH$_4$
Rotation period (days)	155	0.44	0.44
Orbital period (days)	155	0.44	155
Global mean T_S (K)	247.8	273.1	281.9
Dayside mean T_S	273.2	286.7	282.8
Nightside mean T_S	223.9	260.2	281.0
Maximum T_S	296.0	314.2	314.0
Minimum T_S	219.5	230.3	195.8
TOA albedo	0.4895	0.3999	0.3470
Surface albedo	0.1675	0.1109	0.2332
Ice fraction	0.6724	0.5520	0.3053
Cloud fraction (global)	0.4064	0.7342	0.5812
Cloud fraction (dayside)	0.7293	0.7475	0.5803
Cloud fraction (nightside)	0.1014	0.7216	0.5820
Global liquid water cloud mass (g/m^2)	125.9	224.1	136.5
Dayside liquid water cloud mass	257.8	213.2	131.2
Nightside liquid water cloud mass	1.154	234.5	141.8
Global ice water cloud mass	16.13	23.05	16.04
Dayside ice water cloud mass	32.47	24.55	15.53
Nightside ice water cloud mass	0.6916	21.63	16.54
SW cloud forcing (W/m^2)	−130.7	−90.16	−61.56
Global LW cloud forcing	22.94	30.10	25.33
Dayside mean LW cloud forcing	47.46	43.45	24.87
Nightside mean LW cloud forcing	−0.2316	17.49	25.79

Note. For synchronous rotators, the majority of the ice present, which is on the nightside, does not contribute to the surface and top-of-atmosphere (TOA) albedo calculations, as sunlight never touches those regions. The K62 nonsynchronous planet has a larger amount of ice contributing to the surface and TOA albedos than the synchronous planets' (dayside) ice, given that on the nonsynchronous rotator all longitudes of the planet receive sunlight.

all longitudes of the planet receive sunlight over some portion of the planet's 10 hr day, giving rise to a global mean surface temperature that is ∼34 K warmer than on the synchronous K62 planet and ∼9 K warmer than that of the WD planet. However, a larger equator-to-pole temperature difference is evident on the nonsynchronous K62 planet, with a minimum surface temperature that is ∼24 K lower than that on the synchronous K62 planet and ∼35 K lower than that of the WD planet. The nonsynchronous K62 planet's diurnal instellation across all longitudes contributes to both a lower cloud fraction during the planet's day (Figure 8(B)), a lower TOA albedo relative to the synchronous planets (Table 2), and a similar maximum surface temperature to the WD planet.

Where there is ice on the nonsynchronous K62 planet, at upper latitudes as shown in Figure 8(C), the ice has (similar to the K62 synchronous planet) a lower albedo compared to the WD planet which, along with the much stronger LWCF on the planet's nightside (see LWCF nightside mean comparison in Table 2), aids in heat retention, contributing to the higher global mean surface temperature relative to the other two planets. The overall warmer temperatures on the WD planet

and the nonsynchronous K62 planet result in global mean ice fractions that are 18% and 54% lower than on the synchronous K62 planet, respectively. On the synchronous planets, surface ice is concentrated primarily on the nightside, therefore not contributing to the surface and TOA albedo calculations given that sunlight never touches those regions. The K62 nonsynchronous planet has a larger amount of ice contributing to the surface and TOA albedos than the synchronous planets' (dayside) ice, as on the nonsynchronous rotator all longitudes of the planet receive sunlight. This higher fraction of dayside ice is indicative of the much lower minimum surface temperature (∼196 K) on the nonsynchronous K62 planet compared to either of the two synchronous planets. The difference between maximum and minimum surface temperatures increases with decreasing rotation period for the synchronous planets, with the K62 planet exhibiting a ∼74 K difference, compared to an ∼84 K difference on the WD planet. While its global mean, nightside mean, and dayside mean surface temperatures are nearly equivalent, the nonsynchronous K62 planet has the largest max-min surface temperature difference given its larger dayside ice fraction, at ∼118 K, as shown in Figure 9. Relevant values for surface temperature, TOA albedo, and ice fraction are given in Table 2.

4. Discussion

Our comparison of the climates of planets with Earth-like atmospheres and instellations orbiting a main-sequence star and a WD with a similar effective temperature shows remarkable differences resulting from the environments hosting these planets. While minor variations are caused by the small difference in the effective temperatures of the two host stars, which affects the albedos of surface ice and snow on the planets, the major differences in the resulting climates are due to the vastly different rotation periods of the planets, which affect their planetary large- and small-scale atmospheric circulation, cloud concentration and distribution, and strength of the greenhouse effect.

The WD planet is much warmer than the synchronous K62 planet, with a global mean surface temperature that is ∼25 K higher despite having the same solar constant, similar host star SED, and a similar cloud fraction. This contrast is due in part to the increased albedo of thicker, liquid water clouds present on the dayside of the K62 planet, demonstrating the impact of the dayside cloud contribution, given that liquid water clouds contribute most to a planet's TOA albedo (G. L. Stephens et al. 2015). This higher TOA albedo induces the reflection of more SW radiation back to space, cooling temperatures, as indicated by the increased SWCF relative to that of the WD planet. Additionally, the much less efficient cloud and water vapor greenhouse effect on the nightside of the synchronous K62 planet, which has starker, cooler temperatures and a sharply lower mass of ice water clouds, which can contribute more strongly to a planet's greenhouse effect (J. F. B. Mitchell et al. 1989; N. Borduas & N. M. Donahue 2018; J. Bjordal et al. 2020), allows more radiation to escape to space, cooling the planet further.

The surface temperature pattern seen for the WD planet in our study can be called, as has been termed in previous work, a "bat rotator" pattern, constituting a regime of ultrafast orbital period (P < 1 day) within which most WDHZ planets are likely to occupy around their stars (R. Zhan et al. 2024). This much faster relative rotation and orbital period for the
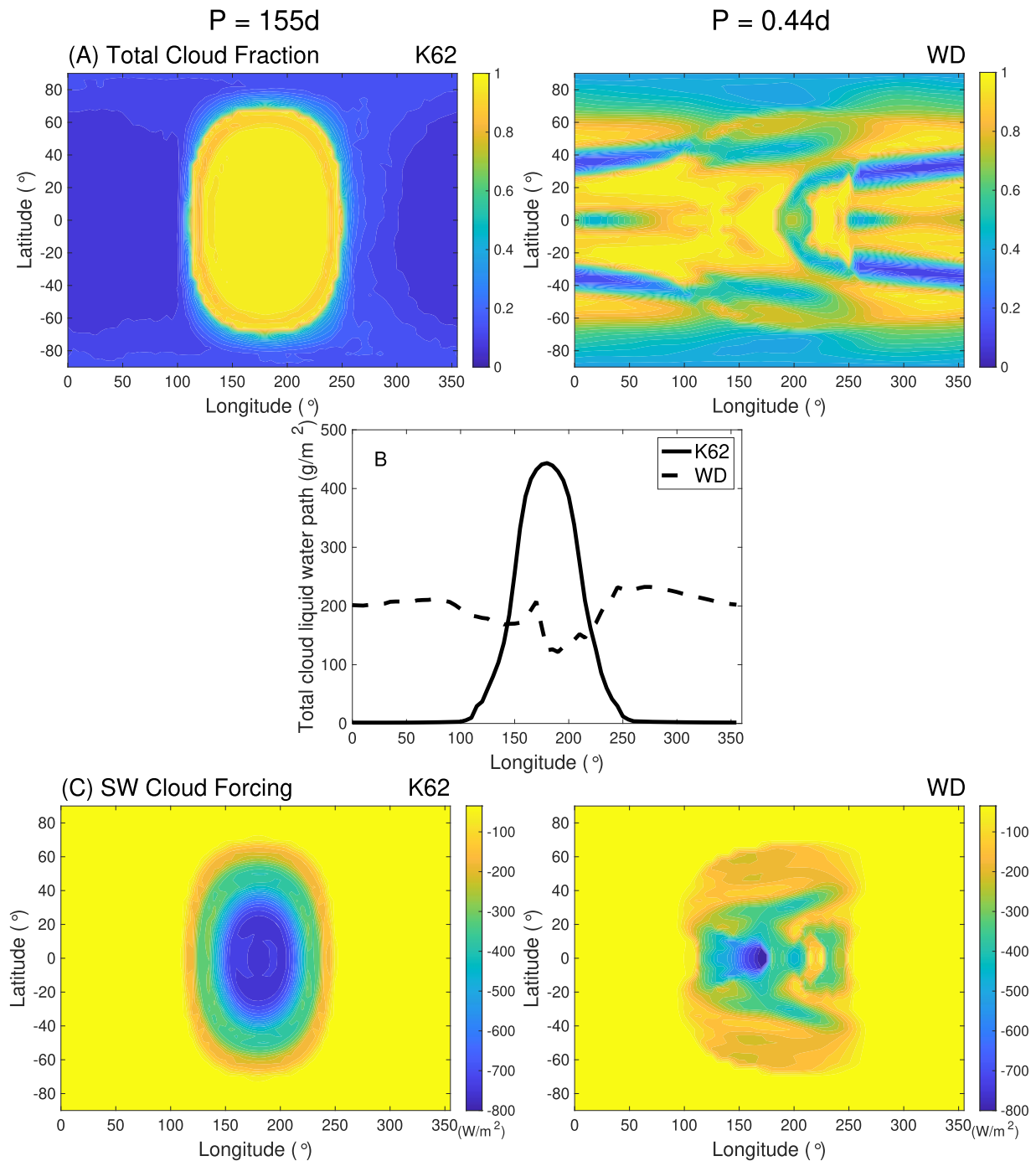
Figure 3. Though the WD planet exhibits higher dayside surface temperatures, the K62 planet has a larger dayside cloud fraction and liquid water cloud mass (Figure 3(A) and latitude-averaged Figure 3(B)), contributing to a stronger (greater net negative) shortwave (SW) cloud forcing and cloud feedback (Figure 3(C)), further cooling temperatures on the K62 planet.

synchronous WD planet stretches out the clouds in the atmosphere, preventing thicker clouds from forming in the same manner as on the K62 planet, generating warmer dayside surface temperatures. K62's slower rotation creates much slower zonal winds and wind convergence at the substellar point, which is the traditional pattern expected on slow, synchronously rotating planets. This pattern allows more clouds to form at the substellar point (see, e.g., M. J. Way et al. 2018; S. D. Guzewich et al. 2020), reflecting more radiation away from the planet via a strong relative stabilizing cloud feedback, often discussed as potentially beneficial for

climate, by buffering close-in planets against runaway greenhouse states (J. Yang et al. 2013, 2014; M. J. Way et al. 2018). While a stabilizing cloud feedback may have a positive effect on planets near the inner edge of their host stars' HZs, where they receive high amounts of instellation that could subject their planets to such runaway greenhouse states, its potential advantage for planets that orbit squarely in the middle of their stars' HZs is lessened, as the net result of this cooling may be to reduce habitable surface area on the planet compared to planets with weaker (smaller net negative) SWCF. Planets occupying an intermediary, "Rhines"
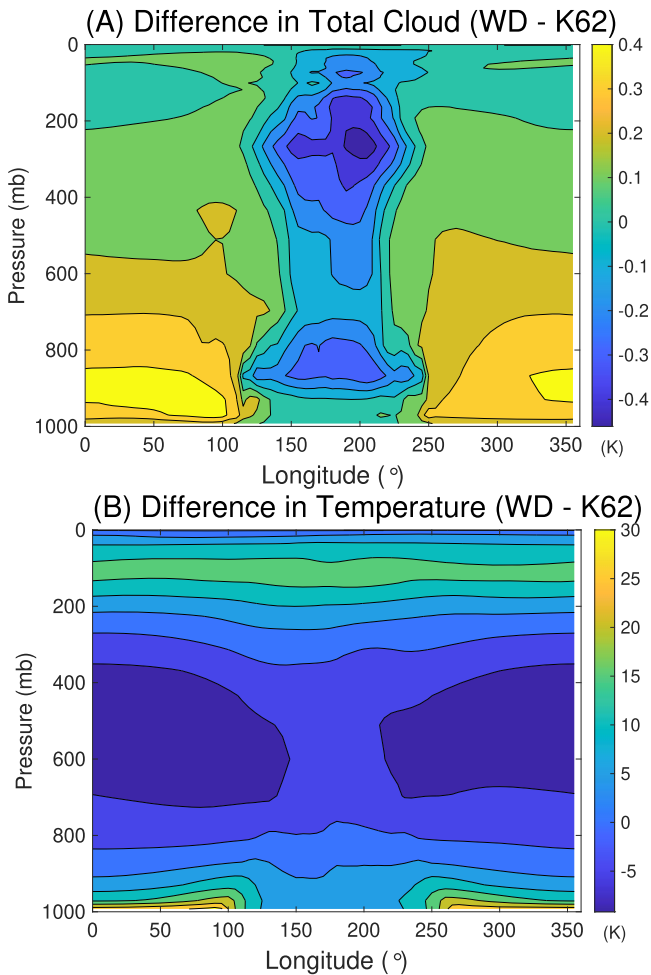
(A) Difference in Total Cloud (WD - K62)

(B) Difference in Temperature (WD - K62)

Figure 4. The WD planet has a lower cloud fraction throughout most of the atmospheric column on the dayside compared to the K62 planet (Figure 4(A)), resulting in less SW heating in these regions, allowing more radiation to make it through the atmosphere to heat the surface of the WD planet (Figure 4(B)).

rotational regime (5 days $< P <$ 20 days; J. Haqq-Misra et al. 2018) between the WD K62 planet's ultrafast rotation and the K62 planet's slow rotation would likely have a stronger stabilizing cloud feedback than that of WD planets given a sharper day–night contrast in atmospheric circulation and resulting larger amount of substellar cloud cover, and occupy a middle range in terms of the advantages and disadvantages of the stabilizing cloud feedback mechanism.

The difference in the amount of surface heating between the two planets certainly impacts habitable surface area, as shown by the ice fraction comparison on both planets (see Table 2). The increased relative heating and lower resultant ice fraction on the WD planet lead to a more optimistic likelihood of deglaciating any frozen planet that may have migrated into the HZ from farther out after the red giant phase (see, e.g., J. H. Debes & S. Sigurdsson 2002) compared to a frozen synchronously rotating planet orbiting a main-sequence star at an equivalent stellar flux distance, particularly if the stabilizing cloud feedback on such slower-rotating synchronous planets, which provides further cooling at close orbital distances (J. Yang et al. 2013), is taken into account.

Surface temperatures reach far below the freezing point of liquid water on the K62 planet's nightside, likely resulting in the condensation of atmospheric water vapor onto the surface.

Long-term evolution of synchronous rotators whose surfaces reach these temperatures could involve the eventual sequestration of water vapor content as ice that could form large glaciers (M. Turbet et al. 2016). However, depending on the planet's gravity and specific properties of the ice (J. Leconte et al. 2013), as well as the planet's geothermal heat flux, which could cause basal melting (K. Menou 2013), such glaciers could migrate to warmer regions of the planet where melting and sublimation back into the atmosphere could occur.

While a warmer surface environment could be more beneficial for life on a WD planet, the closer orbital distances of WDHZ planets, and relatively weaker stabilizing cloud feedback due to their ultrafast rotation, may result in a greater susceptibility to a runaway greenhouse state and associated loss of surface water inventory characteristic of the inner solar system planet Venus (A. P. Ingersoll 1969). The magnitude of potential water loss on WD planets would ultimately depend on initial water inventory and the particular WD's luminosity evolution, as well as the degree of tidal heating (see, e.g., R. Barnes & R. Heller 2013). However, while their shorter orbital and rotation periods reduce dayside cloud coverage and planetary albedo relative to synchronous planets orbiting main-sequence hosts (J. Yang et al. 2014; R. Kopparapu et al. 2016), positioning the runaway greenhouse limit farther away from the star than for slower-rotating synchronous planets orbiting main-sequence stars, WDHZ planets would still rotate synchronously in all likelihood, thereby possessing some degree of stabilizing cloud feedback that reflects incoming SW radiation away from the planet. This latter, shared characteristic between WDHZ and main-sequence synchronous planets (though operating to a weaker degree on WD planets) would place the WD runaway greenhouse limit closer in to the star than for main-sequence stars hosting nonsynchronous, rapidly rotating planets, resulting in a wider HZ for WDs than originally surmised from one-dimensional (1D) studies (R. Zhan et al. 2024). Additionally, moist greenhouse states are less likely on WD planets with ultrafast rotation periods as that in our study, due to drier upper atmospheres compared to planets orbiting main-sequence stars (see, e.g., R. Zhan et al. 2024), as suggested by the lower amount of relative cloud cover shown in Figure 4(A). The susceptibility of WD planets to these aforementioned extremes of climate state at close orbital distances would therefore seem to exist within a similar regime space to that of planets orbiting main-sequence hosts given the somewhat balancing effects of spin synchronization and rotation period.

We assumed a fixed, Earth-like atmosphere in our simulations. Given the early luminous phases of WDs, photolysis of surface H_2O may occur as mentioned above, resulting in the lighter hydrogen escaping to space and the heavier oxygen remaining behind in the atmosphere, as has been proposed to occur on M-dwarf planets during the pre-main-sequence phases of their host stars (see, e.g., R. Luger & R. Barnes 2015). Such oxygenated atmospheres, if present on WD planets, could give rise to increased O_3 production (see, e.g., G. J. Cooke et al. 2022). Previous work exploring the potential impact of the UV environment of WDs on simulated orbiting HZ planets found a substantial decrease in ozone column depth on a hypothetical planet orbiting a 5000 K WD at an equivalent flux distance to that of the Earth around the Sun, resulting in increased UVC radiation reaching the planet's surface, which could be harmful for life (T. Kozakis et al. 2018). However, that study was
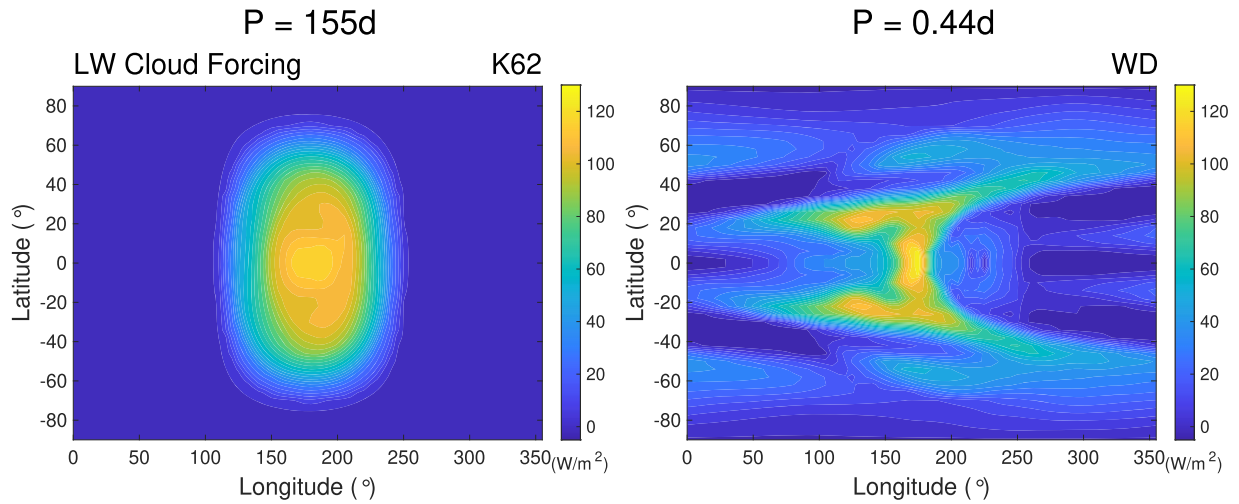
Figure 5. A comparison of the longwave (LW) cloud forcing on the nightsides of both synchronous planets reveals a much stronger contribution of clouds to the WD planet's greenhouse effect compared to the K62 planet, which emits on average ~18 W m^{-2} more radiation to space on its nightside (also see Table 2).
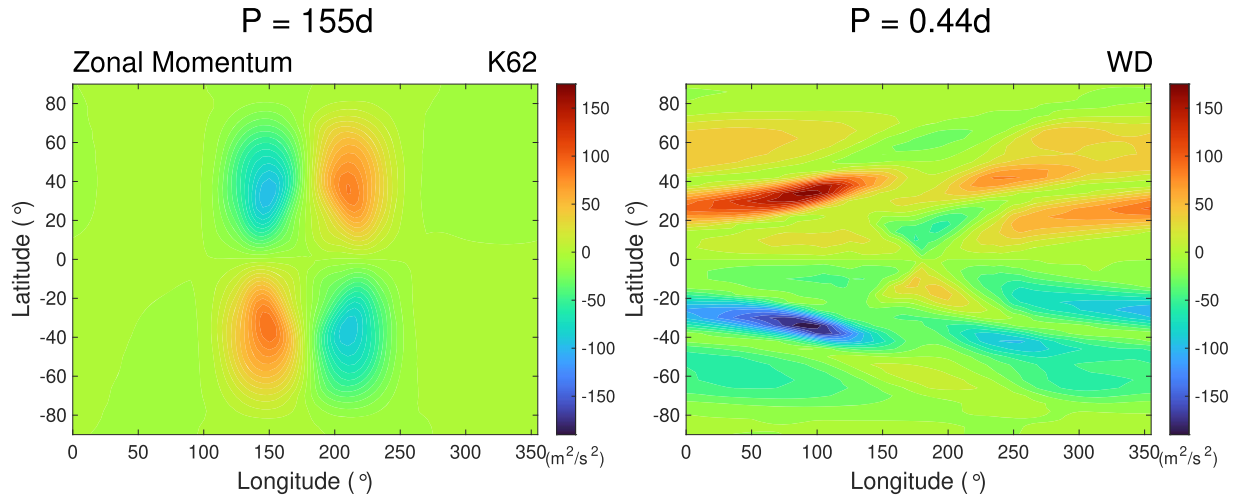

Figure 6. The K62 planet's weaker and symmetrical meridional flux of zonal eddy momentum contributes to a large and relatively uniform cloud fraction centered at the substellar point. In contrast, strong phase tilts above and below the equator on the WD planet transport moisture from higher latitudes, with local minima in the regions of convergence and along the midlatitude zonal wind jets, and local maxima along the phase-tilted directions north and south of the equator, increasing surface temperatures in those regions.
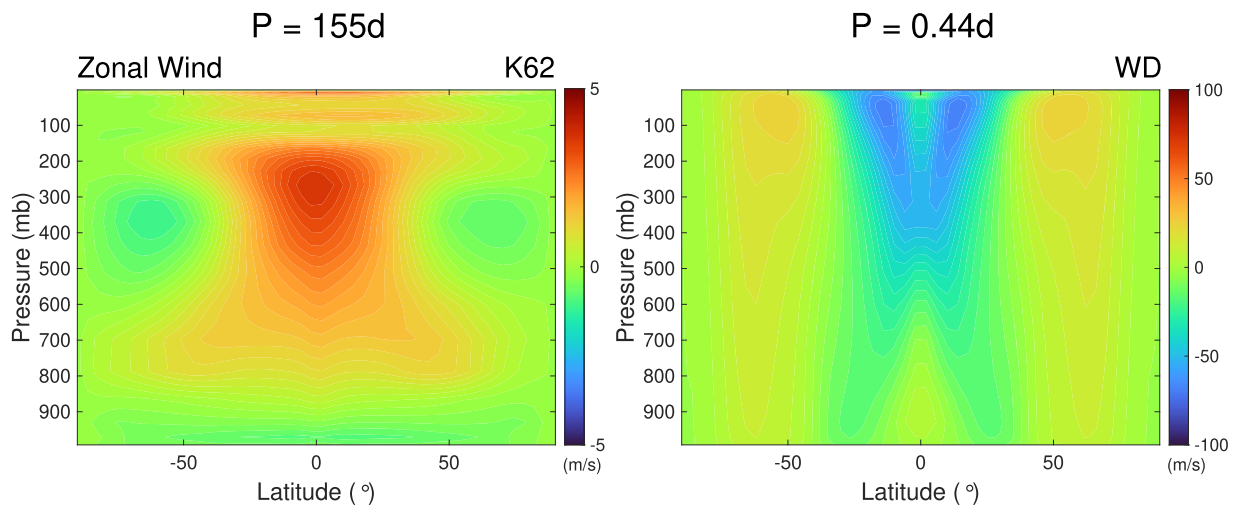
Figure 7. Zonal wind strength is more than an order of magnitude smaller on the slow-rotating K62 planet compared to the WD planet (note different color bar ranges). Equatorial superrotation is present throughout the atmospheric column on the K62 planet, while on the fast-rotating WD planet westward subrotation is present throughout most of the atmospheric column at the equator and subtropics, following the maxima in zonal momentum flux. Eastward equatorial superrotation comprises a small region of the atmosphere below ~500 mb and in the troposphere in the upper latitudes, given that those regions are hotter compared to the equator on the WD planet.
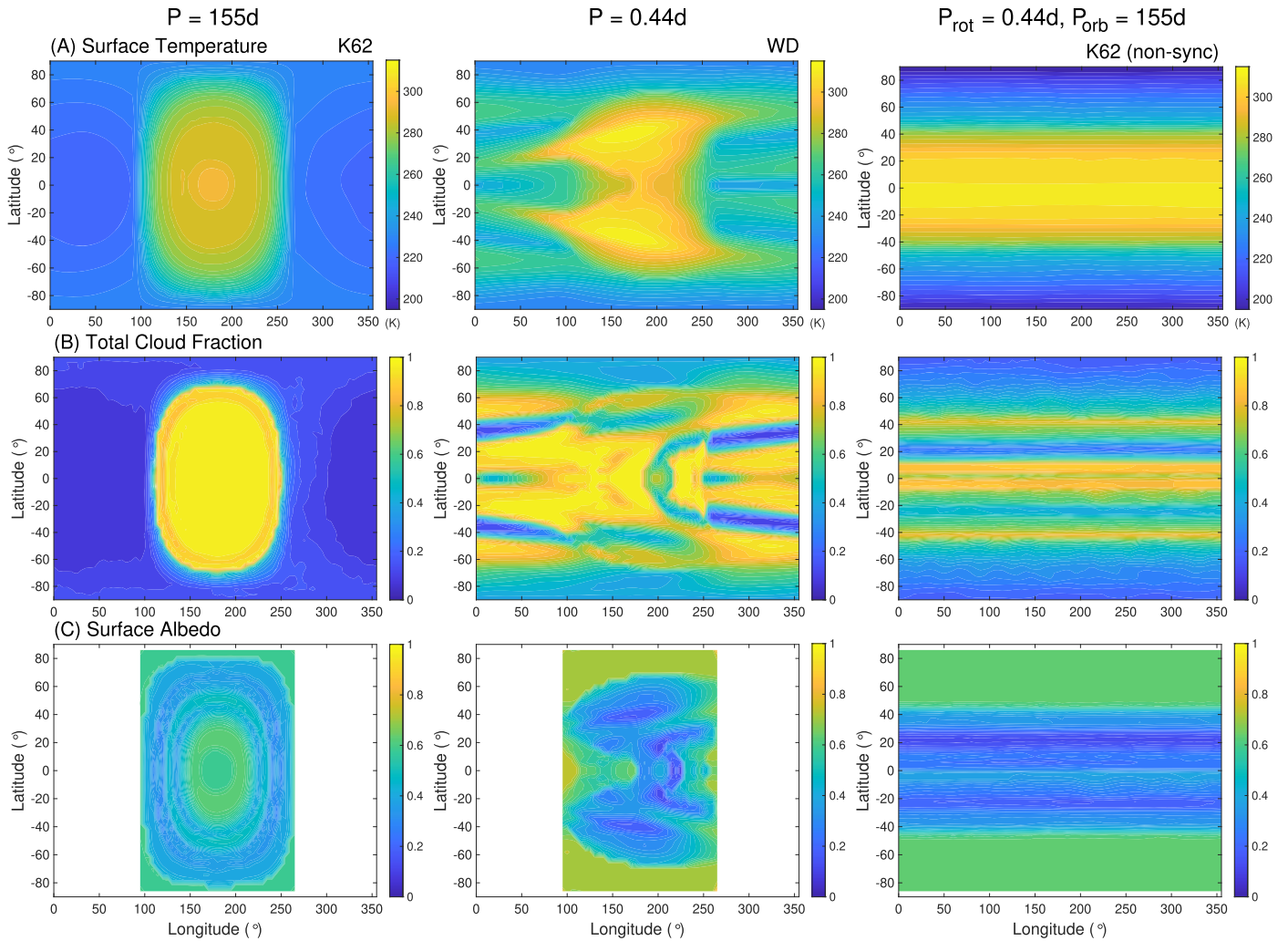
Figure 8. Climate comparison of a nonsynchronous, fast-rotating K62 planet with both synchronous planets. The nonsynchronous K62 planet is warmer overall, with a surface temperature pattern that is longitudinally homogeneous. All longitudes of the planet receive sunlight over some portion of the planet's 10 hr day, giving rise to a lower cloud fraction and a larger amount of ice contributing to the surface and TOA albedos than the synchronous planets' (dayside) ice. This higher fraction of dayside ice on the nonsynchronous planet contributes to a larger equator-to-pole temperature difference compared to either of the synchronous planets, as shown in Figure 8(A). Relevant values for surface temperature, TOA albedo, and ice fraction are given in Table 2.

performed using a 1D radiative-convective model, and did not incorporate what is likely to be a synchronous rotational state for a planet orbiting in the HZ of a WD star, thus garnering much higher global mean surface temperatures for their simulated planet than we find in our study of a synchronous WDHZ planet. Other work exploring the effects of different O_2 concentrations on atmospheric chemistry—finding reductions in CO_2, N_2O, CH_4, O_3, and water vapor column, and subsequent cooling of the troposphere when O_2 levels are reduced (G. J. Cooke et al. 2022)—assumed 24 hr rotation periods. As ozone reactions are temperature sensitive (see, e.g., J. Coates et al. 2016), it would be interesting to see how an accurate surface and atmospheric temperature profile of a WDHZ planet would influence its ozone column depth and shielding for potential life, as greater ozone production would be expected at higher temperatures (J. Coates et al. 2016). Additionally, if greenhouse gases such as CO_2 and CH_4 are present in higher concentrations on WDHZ planets given their potentially oxygenated atmospheres, the additional atmospheric absorption is likely to result in higher surface temperatures than we calculated here for all planets. We would expect the atmospheric heating to be slightly higher on the K62 planet,

due to its host star's slightly cooler effective temperature, resulting in a small increase in the near-IR radiation contribution to its spectrum relative to the WD (see Figure 1) and associated atmospheric greenhouse gas absorption. Increased greenhouse gas concentrations could further buffer WD planets against global glaciations, though may be more advantageous for nonsynchronous planets orbiting main-sequence stars farther out in their host stars' HZs.

For main-sequence stars, the range of climates possible for HZ planets is far greater given the many potential rotational-orbital spin states, as shown by our comparison of the synchronous and nonsynchronous planet simulations. What seems clear is that a HZ planet found around a WD star is more likely to be warm given its expected synchronous spin state. A nonsynchronous HZ planet orbiting a main-sequence star, despite an equally fast rotation period, is likely to carry some climatic advantages if its orbital period is much longer, including a lower amount of reflective cloud cover, a stronger nightside greenhouse effect, and lower-albedo ice surfaces if its host star has an even slightly cooler effective temperature, all of which contribute to a warmer environment than that of the (synchronously rotating) WDHZ planet, though with colder
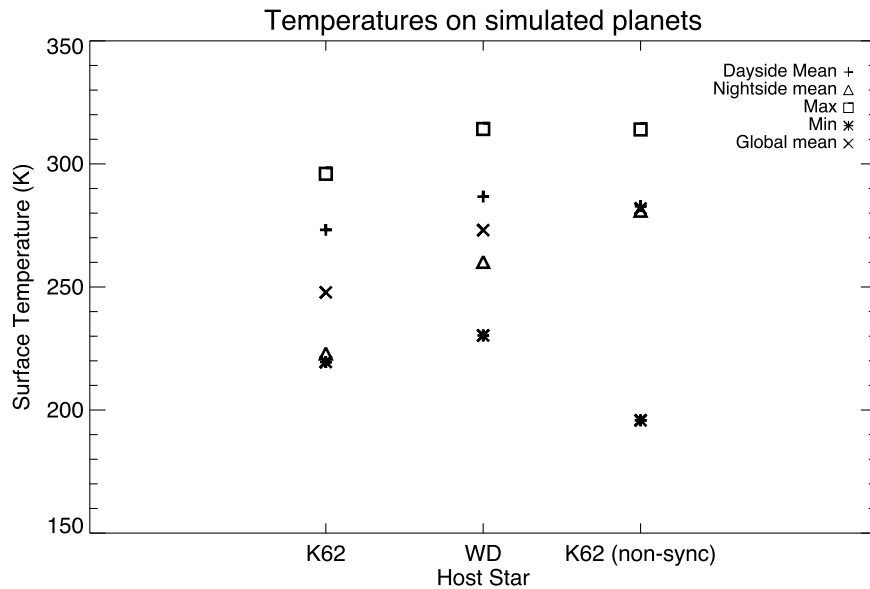
Figure 9. While the nonsynchronous planet exhibits a larger difference between maximum and minimum surface temperatures compared to either of the synchronous planets, with colder upper-latitude regions given the amount of ice exposed to sunlight throughout the planet's day, it also has global mean, dayside mean, and nightside mean surface temperatures that are nearly equivalent to each other, in large part due to a lower relative amount of reflective cloud cover and a strong nightside greenhouse effect.

poles and upper-latitude regions given the amount of ice exposed to sunlight throughout the planet's day in the nonsynchronous case. However, the WD planet's fast 1:1 spin–orbit period, which generates strong and phase-tilted meridional flux of zonal momentum and extended scales of cloud cover and atmospheric circulation, would seem to narrow this climatic gap compared to that between nonsynchronous and synchronous planets orbiting a main-sequence star (see Table 2).

As it is likely that many of the planets orbiting WD progenitors will have been engulfed during the red giant phase, WD planets may be few within their systems, and possibly orbiting alone in single-planet systems. Other work has shown that (previously) spin-synchronized planets orbiting at the outer edge of the HZ in compact multiple-planet systems are more susceptible to global-scale glaciations, due to gravitationally induced libration of the substellar point away from open ocean basins on these planets (H. Chen et al. 2023). H. Chen et al. (2023) found that planets orbiting closer in to their stars within the HZ of these compact systems are less susceptible to these substellar longitude migrations resulting from gravitational perturbations by planetary companions, and that these effects are, naturally, nonexistent in single-planet systems. As other recent work has found planets in the 0.1–$2R_\oplus$ range orbiting in the HZ of WDs to be an order of magnitude lower in occurrence than larger (2–$20R_\oplus$) planets (D. Kipping 2024), and evidence of circumstellar disk material around WDs could be indicative of the tidal disruption of any planets that did originally survive the red giant phase (see, e.g., A. Aungwerojwit et al. 2024), WDHZ planets may indeed be few or single around WDs, and therefore more robust against such snowball states due to their extremely close orbital distances given their host stars' luminosities, which all but ensure a consistently fixed substellar point.

While the 10 hr synchronous rotational and orbital period of our hypothetical WD planet lies at the other extreme compared to that of a synchronous HZ planet orbiting a main-sequence star, the stretched out scales often seen in this fast-rotating

regime in simulations of terrestrial planets (see, e.g., A. P. Showman & L. M. Polvani 2011; Y. Kaspi & A. P. Showman 2015; J. Haqq-Misra et al. 2018; T. D. Komacek & D. S. Abbot 2019; S. D. Guzewich et al. 2020), and comparatively diminished SWCF and enhanced LWCF pose the advantage of allowing such planets to retain more of the heat from their stars, even as their expired nuclear furnaces continue to cool over time. However, an additional counterpoint to this potential advantage exists, as early in the evolutionary stage of a WD, when it is more luminous, orbiting close-in planets that are already warm would be rendered even hotter, which could reduce habitable surface area. Our understanding of the ultimate habitability potential of WD planets would benefit from future studies that incorporate the time-evolving HZ of a WD to explore the evolution of a rocky planet's climate sensitivity as its host star's stellar flux decreases over time, though this would require the incorporation of a carbonate-silicate cycle, which regulates silicate weathering and planetary surface temperature (J. C. G. Walker et al. 1981). Regardless, the results of the study presented here suggest that the WD stellar environment, once dismissed as unimaginable for life, may present a newfound consideration for observational efforts in search of habitable planets in the coming decades.

5. Conclusions

We used a 3D GCM to simulate the climates of synchronously rotating planets with Earth-like atmospheres and instellations orbiting in the HZs of a 5000 K WD star and main-sequence K-dwarf star K62 of similar effective temperature. We have shown their markedly differing climates to be largely due to the rotation periods of the two planets at their respective orbital distances. While the much slower, 155 day rotation and orbital period of the planet orbiting K62 exhibits a large dayside liquid water cloud mass, SW cloud forcing, and TOA albedo, along with a weakened nightside greenhouse effect, the WD planet's much faster, 10 hr rotation and orbital

period generates strong zonal winds that stretch out the atmospheric and cloud circulation across the planet, fewer dayside liquid water clouds, and a stronger greenhouse effect on the nightside, contributing to a global mean surface temperature that is ~25 K higher than that of the K62 planet. In the nonsynchronous case for the planet orbiting K62 with the 10 hr rotation period of the WD planet, the larger fraction of surface ice that is exposed to sunlight over all longitudes, though lower-albedo ice compared to that of the WD planet, generates an overall warmer surface environment, albeit with lower temperatures in the upper latitudes and at the poles. That the strong and homogeneous atmospheric circulation of the WD planet compensates for much of the increased warming on the nonsynchronous planet has important implications for future exoplanet characterization efforts. The potential climates of planets that formed within or migrated to the HZs of WD stars may be more accurately assessed prior to direct observational confirmation of their spin states, as they are more likely to exist in a synchronous rotation state, provide warmer surface temperatures than synchronous planets orbiting main-sequence stars, and have comparable surface temperatures even to nonsynchronous, rapidly rotating planets orbiting main-sequence stars. WDHZ planets may therefore harbor more clement conditions for life to compensate for the cooling and dimming of their host stars over time.

Acknowledgments

ORCID iDs

Aomawa L. Shields ● https://orcid.org/0000-0002-7086-9516
Eric T. Wolf ● https://orcid.org/0000-0002-7188-1648
Eric Agol ● https://orcid.org/0000-0002-0802-9145
Pier-Emmanuel Tremblay ● https://orcid.org/0000-0001-9873-0121

References

Agol, E. 2011a, ApJL, 731, L31
Agol, E. 2011b, in Telescopes from Afar, Proc. Conf., ed. S. Gajadhar et al. (Waikoloa Beach, HI: TFA), 25
Aungwerojwit, A., Gänsicke, B. T., Dhillon, V. S., et al. 2024, MNRAS, 530, 117
Barnes, R. 2017, CeMDA, 129, 509
Barnes, R., & Heller, R. 2013, AsBio, 13, 279
Bédard, A., Bergeron, P., Brassard, P., & Fontaine, G. 2020, ApJ, 901, 93
Bédard, A., Brassard, P., Bergeron, P., & Blouin, S. 2022, ApJ, 927, 128
Bergeron, P., Saumon, D., & Wesemael, F. 1995a, ApJ, 443, 764
Bergeron, P., Wesemael, F., & Beauchamp, A. 1995b, PASP, 107, 1047
Bitz, C. M., Holland, M. M., Weaver, A. J., & Eby, M. 2001, JGRC, 106, 2441
Bjordal, J., Storelvmo, T., Alterskjær, K., & Carlsen, T. 2020, NatGe, 13, 718
Blackman, J. W., Beaulieu, J. P., Bennett, D. P., et al. 2021, Natur, 598, 272
Borduas, N., & Donahue, N. M. 2018, in Green Chemistry, ed. B. Török & T. Dransfield (Amsterdam: Elsevier), 131
Carns, R. C., Brandt, R. E., & Warren, S. G. 2015, JGRC, 120, 7400
Carns, R. C., Light, B., & Warren, S. G. 2016, JGRC, 121, 5217
Chen, H., Li, G., Paradise, A., & Kopparapu, R. K. 2023, ApJL, 946, L32
Chen, J., Ferraro, F. R., Cadelano, M., et al. 2021, NatAs, 5, 1170
Coates, J., Mar, K. A., Ojha, N., & Butler, T. M. 2016, ACP, 16, 11601
Cooke, G. J., Marsh, D. R., Walsh, C., Rugheimer, S., & Villanueva, G. L. 2022, MNRAS, 518, 206
Debes, J. H., & Sigurdsson, S. 2002, ApJ, 572, 556
Dunkle, R. V., & Bevans, J. T. 1956, JMetR, 13, 212
Edson, A., Lee, S., Bannon, P., Kasting, J. F., & Pollard, D. 2011, Icar, 212, 1
Farihi, J., Hermes, J. J., Marsh, T. R., et al. 2022, MNRAS, 511, 1647
Fossati, L., Bagnulo, S., Haswell, C. A., et al. 2012, ApJL, 757, L15
Fulton, B. J., & Petigura, E. A. 2018, AJ, 156, 264
Gänsicke, B. T., Schreiber, M. R., Toloza, O., et al. 2019, Natur, 576, 61
Gardner, J. P., Mather, J. C., Clampin, M., et al. 2006, SSRv, 123, 485
Gent, P. R., Danabasoglu, G., Donner, L. J., et al. 2011, JCli, 24, 4973
Gertz, J. 2019, JBIS, 72, 386
Guzewich, S. D., Lustig-Yaeger, J., Davis, C. E., et al. 2020, ApJ, 893, 140
Haqq-Misra, J., Wolf, E. T., Joshi, M., Zhang, X., & Kopparapu, R. k. 2018, ApJ, 852, 67
Hu, Y., & Yang, J. 2014, PNAS, 111, 629
Hunke, E. C., & Lipscomb, W. H. 2008, CICE: The Los Alamos Sea Ice Model. Documentation and Software User's Manual. Version 4.0. Tech. Rep. LA-CC-06-012, T-3 Fluid Dynamics Group, Los Alamos National Laboratory
Ingersoll, A. P. 1969, JAtS, 26, 1191
Joshi, M. M., & Haberle, R. M. 2012, AsBio, 12, 3
Jura, M. 2003, ApJL, 584, L91
Kalirai, J. 2018, ConPh, 59, 251
Kaltenegger, L., MacDonald, R. J., Kozakis, T., et al. 2020, ApJL, 901, L1
Kaspi, Y., & Showman, A. P. 2015, ApJ, 804, 60
Kipping, D. 2024, MNRAS, 527, 3532
Kite, E. S., Gaidos, E., & Manga, M. 2011, ApJ, 743, 41
Komacek, T. D., & Abbot, D. S. 2019, ApJ, 871, 245
Komacek, T. D., Jansen, M. F., Wolf, E. T., & Abbot, D. S. 2019, ApJ, 883, 46
Kopparapu, R. k., Wolf, E. T., Haqq-Misra, J., et al. 2016, ApJ, 819, 84
Kowalski, P. M., & Saumon, D. 2006, ApJL, 651, L137
Kozakis, T., Kaltenegger, L., & Hoard, D. W. 2018, ApJ, 862, 69
Lane, M. D., & Christensen, P. R. 1998, Icar, 135, 528
Leconte, J., Forget, F., Charnay, B., Wordsworth, R., & Pottier, A. 2013, Natur, 504, 268
Leconte, J., Wu, H., Menou, K., & Murray, N. 2015, Sci, 347, 632
Light, B., Carns, R. C., & Warren, S. G. 2016, JGRC, 121, 4966
Lin, Z., Seager, S., Ranjan, S., Kozakis, T., & Kaltenegger, L. 2022, ApJL, 925, L10
Livio, M., Pringle, J. E., & Wood, K. 2005, ApJL, 632, L37
Lobo, A. H., Shields, A. L., Palubski, I. Z., & Wolf, E. 2023, ApJ, 945, 161
Loeb, A., & Maoz, D. 2013, MNRAS, 432, L11
Luger, R., & Barnes, R. 2015, AsBio, 15, 119
Luhman, K. L., Burgasser, A. J., & Bochanski, J. J. 2011, ApJL, 730, L9
Menou, K. 2013, ApJ, 774, 51
Mitchell, J. F. B., Senior, C. A., & Ingram, W. J. 1989, Natur, 341, 132
Mullally, S. E., Debes, J., Cracraft, M., et al. 2024, ApJL, 962, L32
Nordhaus, J., Spiegel, D. S., Ibgui, L., Goodman, J., & Burrows, A. 2010, MNRAS, 408, 631
Oppenheimer, B. R., Saumon, D., Hodgkin, S. T., et al. 2001, ApJ, 550, 448
Ostriker, J. P., & Axel, L. 1968, AJS, 73, 31
Palubski, I., Shields, A., & Deitrick, R. 2020, ApJ, 890, 30
Rushby, A. J., Shields, A. L., & Joshi, M. 2019, ApJ, 887, 29
Rushby, A. J., Shields, A. L., Wolf, E. T., Laguë, M., & Burgasser, A. 2020, ApJ, 904, 124
Shields, A. L., Barnes, R., Agol, E., et al. 2016, AsBio, 16, 443
Shields, A. L., Bitz, C. M., Meadows, V. S., Joshi, M. M., & Robinson, T. D. 2014, ApJL, 785, L9
Shields, A. L., & Carns, R. C. 2018, ApJ, 867, 11
Shields, A. L., Meadows, V. S., Bitz, C. M., et al. 2013, AsBio, 13, 715

Showman, A. P., & Polvani, L. M. 2011, ApJ, 738, 71
Showman, A. P., Wordsworth, R. D., Merlis, T. M., & Kaspi, Y. 2013, in Atmospheric Circulation of Terrestrial Exoplanets, ed. S. J. Mackwell et al. (Tucson, AZ: Univ. Arizona Press), 94
Sigurdsson, S., Richer, H. B., Hansen, B. M., Stairs, I. H., & Thorsett, S. E. 2003, Sci, 301, 193
Stephens, G. L., O'Brien, D., Webster, P. J., et al. 2015, RvGeo, 53, 141
Swan, A., Farihi, J., Su, K. Y. L., & Desch, S. J. 2024, MNRAS, 529, L41
Thorsett, S. E., Arzoumanian, Z., & Taylor, J. H. 1993, ApJL, 412, L33
Tremblay, P. E., Bergeron, P., & Gianninas, A. 2011, ApJ, 730, 128
Turbet, M., Leconte, J., Selsis, F., et al. 2016, A&A, 596, A112
Vanderbosch, Z., Hermes, J. J., Dennihy, E., et al. 2020, ApJ, 897, 171
Vanderburg, A., Johnson, J. A., Rappaport, S., et al. 2015, Natur, 526, 546
Vanderburg, A., Rappaport, S. A., Xu, S., et al. 2020, Natur, 585, 363

Veras, D. 2021, Oxford Research Encyclopedia of Planetary Science (Oxford: Oxford Univ. Press), 1
Walker, J. C. G., Hays, P. B., & Kasting, J. F. 1981, JGRC, 86, 9776
Wang, Y., Tian, F., & Hu, Y. 2014a, ApJL, 791, L12
Wang, Y., Tian, F., & Hu, Y. 2014b, ApJL, 791, L42
Way, M. J., Genio, A. D. D., Aleinov, I., et al. 2018, ApJS, 239, 24
Williams, D. M., & Pollard, D. 2003, IJAsB, 2, 1
Winget, D. E., Hansen, C. J., Liebert, J., et al. 1987, ApJL, 315, L77
Wolf, E. T., Kopparapu, R., Haqq-Misra, J., & Fauchez, T. J. 2022, PSJ, 3, 7
Wordsworth, R. D., Forget, F., Selsis, F., et al. 2010, A&A, 522, A22
Yang, J., Boué, G., Fabrycky, D. C., & Abbot, D. S. 2014, ApJL, 787, L2
Yang, J., Cowan, N. B., & Abbot, D. S. 2013, ApJL, 771, L45
Zhan, R., Koll, D. D. B., & Ding, F. 2024, ApJ, 971, 125
Zhang, K., Zang, W., El-Badry, K., et al. 2024, NatAs, 8, 1575